We are IntechOpen,
the world's leading publisher of Open Access books
Built by scientists, for scientists

6,900
Open access books available

186,000
International authors and editors

200M
Downloads

Our authors are among the

154
Countries delivered to

TOP 1%
most cited scientists

12.2%
Contributors from top 500 universities

CLARIVATE ANALYTICS
BOOK CITATION INDEX
INDEXED

WEB OF SCIENCE™

Selection of our books indexed in the Book Citation Index
in Web of Science™ Core Collection (BKCI)

Interested in publishing with us?
Contact book.department@intechopen.com

Introducing Ohmic Contacts into Silicon Carbide Technology

Zhongchang Wang, Susumu Tsukimoto,
Mitsuhiro Saito and Yuichi Ikuhara
WPI Research Center, Advanced Institute for Materials Research, Tohoku University
2-1-1 Katahira, Aoba-ku,
Japan

1. Introduction

The promising mechanical and electronic properties of silicon carbide (SiC) are stimulating extensive investigations focused on the applications of its semiconducting and excellent structure properties. As a matter of fact, the interest toward SiC is twofold. On one hand, it is a high-strength composite and high-temperature structural ceramic, demonstrating the ability to function at high-power and caustic circumstances. On the other hand, it is an attractive semiconductor, which has excellent inherent characteristics such as a wide band gap (3.3 eV), high breakdown field (3×10^6 V/cm), more than double the high carrier mobility and electron saturation drift velocity (2.7×10^7 cm/s) of silicon (Morkoc et al., 1994). These intrinsic electronic properties together with the high thermal conductivity (5 W/cm K) and stability make it the most likely of all wide-band-gap semiconductors to succeed the current Si and GaAs as next-generation electronic devices, especially for high-temperature and high-frequency applications. Successful fabrication of SiC-based semiconductor devices includes Schottky barrier diodes, p-i-n diodes, metal-oxide-semiconductor field effect transistors, insulated gate bipolar transistors and so forth. Moreover, current significant improvements in its epitaxial and bulk crystal growth have paved the way for fabricating its electronic devices, which arouses further interest in developing device processing techniques so as to take full advantage of its superior inherent properties.

One of the most critical issues currently limiting its device processing and hence its widespread application is the manufacturing of reliable and low-resistance Ohmic contacts ($< 1 \times 10^{-5}$ Ωcm^2), especially to p-type SiC (Perez-Wurfl et al., 2003). The Ohmic contacts are primarily important in SiC devices because a Schottky barrier of high energy is inclined to form at an interface between metal and wide-band-gap semiconductor, which consequently results in low-current driving, slow switching speed, and increased power dissipation. Much of effort expended to date to realize the Ohmic contact has mainly focused on two techniques. One is the high-dose ion-implantation approach, which can increase the carrier density of SiC noticeably and lower its depletion layer width significantly so that increasing tunnelling current is able to flow across barrier region. Although the doping layers with high concentration ($> 10^{20}$ cm^{-3}) were formed, the key problem of this method is the easy formation of lattice defects or amorphization during the ion implantation. These defects are unfortunately very stable and need to be recovered via post-annealing at an extremely high temperature (~ 2000 K), thereby complicating mass production of SiC devices.

The other alternative is to generate an intermediate semiconductor layer with narrower band gap or higher carrier density at the contacts/SiC interface by deposition and annealing technique. To form such layers, many materials have been examined in a trial-and-error designing fashion, including metals, silicides, carbides, nitrides, and graphite. Of all these materials, metallic alloys have been investigated extensively, largely because the fabrication process is simple, standard, and requires no exotic substances. In particular, most of research activities have been focused on TiAl-based alloys, the only currently available materials that yield significantly low contact resistance (Ohmic contact) to the *p*-type SiC. Furthermore, they demonstrate high thermal stability. For example, Tanimoto et al. have developed the TiAl contacts with extremely low specific contact resistance in the range of 10^{-7} to 10^{-6} Ωcm^2 for the *p*-type 4H-SiC with an Al doping concentration of 1.2×10^{19} cm^{-3} (Tanimoto et al., 2002). Although a lot of intriguing results have been obtained regarding the TiAl-based contact systems, the mechanism whereby the Schottky becomes Ohmic after annealing has not been well clarified yet. In other words, the key factors to understanding the formation of origin of Ohmic contact remains controversial. Mohney et al. proposed that a high density of surface pits and spikes underneath the contacts contributes to the formation of Ohmic behaviour based on their observations using the scanning electron microscopy and atomic force microscopy (Mohney et al., 2002). Nakatsuka et al., however, concluded that the Al concentration in the TiAl alloys is fundamental for the contact formation (Nakatsuka et al., 2002). Using the liquid etch and ion milling techniques, John & Capano ruled out these possibilities and claimed that what matters in realizing the Ohmic nature is the carbides, Ti_3SiC_2 and Al_4C_3, formed between metals and semiconductor(John & Capano, 2004). This, however, differs, to some extent, from the X-ray diffraction (XRD) observations revealing that the compounds formed at the metal/SiC interface are silicides, $TiSi_2$, TiSi and Ti_3SiC_2 (Chang et al., 2005). The formation of silicides or carbides on the surface of SiC substrate after annealing may serve as a primary current-transport pathway to lower the high Schottky barrier between the metal and the semiconductors. In addition, Ohyanagi et al. argued that carbon exists at the contacts/SiC interface and might play a crucial role in lowering Schottky barrier (Ohyanagi et al., 2008). These are just a few representative examples illustrating the obvious discrepancies in clarifying the formation mechanism of Ohmic contact. Taking the amount of speculations on the mechanism and the increasing needs for better device design and performance control, understanding the underlying formation origin is timely and relevant.

To develop an understanding of the origin in such a complex system, it is important to focus first on microstructure characterization. Tanimoto et al. examined the microstructure at the interface between TiAl contacts and the SiC using Auger electron spectroscopy and found that carbides containing Ti and Si were formed at interface (Tanimoto et al., 2002). Recently, transmission electron microscopy (TEM) studies by Tsukimoto et al. have provided useful information in this aspect due to possible high-resolution imaging (Tsukimoto et al., 2004). They have found that the majority of compounds generated on the surface of 4H-SiC substrate after annealing consist of a newly formed compound and hence proposed that the new interface is responsible for the lowering of Schottky barrier in the TiAl-based contact system. However, role of the interface in realizing the Ohmic nature remains unclear. It is not even clear how the two materials bond together atomically from these experiments, which is very important because it may strongly affect physical properties of the system.

To determine the most stable interface theoretically, one first has to establish feasible models on the basis of distinct terminations and contact sites and then compare them. However, a

direct comparison of the total energies of such models is not physically meaningful since interfaces might have a different number of atoms. On the other hand, the ideal work of adhesion, or adhesion energy, W_{ad}, which is key to predicting mechanical and thermodynamic properties of an interface is physically comparable. Generally, the W_{ad}, which is defined as reversible energy required to separate an interface into two free surfaces, can be expressed by the difference in total energy between the interface and isolated slabs,

$$W_{ad} = (E_1 + E_2 - E_{IF})/A. \tag{1}$$

Here E_1, E_2, and E_{IF} are total energies of isolated slab 1, slab 2, and their interface system, respectively, and A is the total interface area. To date, analytic models available for predicting W_{ad} concerning SiC have mostly been restricted to SiC/metal heterojctions such as SiC/Ni, SiC/Al and SiC/Ti. These models are motivated by the experimental deposition of metals on SiC. However, they neglect the complexity of situation; namely, the compounds (silicides or carbides) can be generated on SiC substrate after annealing and thus the models are only applicable to systems with as-deposited state.

Recent advances in the high-angle annular-dark-field (HAADF) microscopy, the highest resolution, have enabled an atomic-scale imaging of a buried interface (Nellist et al., 2004). However, a direct interpretation of the observed HAADF images is not always straightforward because there might be abrupt structural discontinuity, mixing of several species of elements on individual atomic columns, or missing contrasts of light elements. One possible way out to complement the microscopic data is via atomistic calculation, especially the first-principles calculation. As well known, the atomistic first-principles simulations have long been confirmed to be able to suggest plausible structures, elucidate the reason behind the observed images, and even provide a quantitative insight into how interface governs properties of materials. Consequently, a combination of state-of-the-art microcopy and accurate atomistic modeling is an important advance for determining interface atomic-scale structure and relating it to device properties, revealing, in this way, physics origin of contact issues in SiC electronics.

In addition to determining atomic structure of 4H-SiC/Ti$_3$SiC$_2$ interface, the goal of this chapter is to clarify formation mechanism of the TiAl-based Ohmic contacts so as to provide suggestions for further improvement of the contacts. 4H-SiC will hereafter be referred to as SiC. First of all, we fabricated the TiAl-based contacts and measured their electric properties to confirm the formation of Ohmic contact. Next, the metals/SiC interface was analyzed using the XRD to identify reaction products and TEM, high-resolution TEM (HRTEM), and scanning TEM (STEM) to observe microstructures. Based on these observations, we finally performed systematic first-principles calculations, aimed at assisting the understanding of Ohmic contact formation at a quantum mechanical level. The remainder of this chapter is organized as follows: Section 2 presents the experimental procedures, observes the contact microstructure, and determines the orientation relationships between the generated Ti$_3$SiC$_2$ and SiC substrate. Section 3 describes the computational method, shows detailed results on bulk and surface calculations, outlines the geometries of the 96 candidate interfaces, and determine the structure, electronic states, local bonding, and nonequilibrium quantum transport of the interface. We provide disscussion and concluding remarks in Sec. 4.

2. Experimental characterization

The *p*-type 4H-SiC epitaxial layers (5-μm thick) doped with aluminum ($N_A = 4.5 \times 10^{18}$ cm^{-3}) which were grown on undoped 4H-SiC wafers by chemical vapor deposition (manufactured

by Cree Research, Inc.) were used as substrates. The 4H-SiC substrates had 8°-off Si-terminated (0001) surfaces inclined toward a [-2110] direction because only 4H-type structure of SiC with polymorph (e.g. 3C, 4H, 6H, 15R etc.) was controllable by lateral growth of the epitaxial layers parallel to (0001)-oriented surface. After chemical cleaning of the substrate surface, a 10 nm-thick sacrificial oxide (SiO_x) layer was grown on the SiC substrate by dry-oxidation at 1423 K for 60 min. The electrode patterns were made by removing the SiO_x layers, where contact metals were deposited by dipping in 5 % diluted hydrofluoric acid solution for 1 min using a photolithography technique. Prior to the deposition of contact materials, the substrates were cleaned by deionized water. Then, Ti and Al stacking layers with high purities were deposited sequentially on the substrate in a high vacuum chamber where the base pressure was below 5×10^{-6} Pa. The thicknesses of the Ti and Al layers investigated in this study are 100 nm and 380 nm, respectively, and these layer thicknesses were chosen to give the average composition of the Ti(20 at%) and Al(80 at%), where the layer thicknesses were measured by a quartz oscillator during deposition. The reasons to choose this average composition was that aluminum rich (more than 75 at%) in TiAl contacts were empirically found to be essential to yield low contact resistance, resulting from formation of the Ti_3SiC_2 compound layers. After depositing, the binary TiAl contact layers were annealed at 1273 K for a storage time of 2 min in an ultra-high vacuum chamber where the vacuum pressure was below 1×10^{-7} Pa.

The surface morphology of the TiAl contact layers on 4H-SiC after annealing was observed using a JEOL JSM-6060 scanning electron microscope (SEM). Microstructural analysis and identification of the Ti_3SiC_2 layers at the contact layers/4H-SiC interfaces after annealing was performed using X-ray diffraction (XRD) and cross-sectional TEM. For XRD analysis, Rigaku RINT-2500 with Cu *Ka* radiation operated at 30 kV and 100 mA was used. In particular, the interfacial structures and an orientation relationship between the contact layers and the 4H-SiC substrates were characterized by cross-sectional high-resolution TEM observations and selected area diffraction pattern (SADP) analysis, respectively, using a JEOL JEM-4000EX electron microscope operated at an accelerating voltage of 400 kV, where the point-to-point resolution of this microscope was approximately 0.17 nm. Z-contrast images were obtained using a spherical aberration (C_s) corrected scanning transmission electron microscope (STEM) (JEOL 2100F), which provides an unprecedented opportunity to investigated atomic-scale structure with a sub-Å electron probe. Thin foil specimens for the TEM and STEM observations were prepared by the standard procedures: cutting, gluing, mechanical grinding, dimple polishing, and argon ion sputter thinning techniques.

2.1 Formation of Ohmic contacts

To verify the formation of Ohmic contact, we measured the electric properties ($I-V$ characteristics) for the TiAl contact systems before and after annealing (Fig. 1). For the system before annealing, its current almost maintains zero despite that the applied bias ranges from −3.0 to 3.0 V, which unambiguously reflects Schottky character of this system. This can be understood by considering that the potential induced by applied bias drops largely at an contact interface between metals and semiconductors, thus hindering the current flow. The annealed system, however, exhibits a typical Ohmic nature, as its $I-V$ curve is nearly linear and the current increases sharply with the rise of applied bias. This drastic change of electric properties suggests that there might be substantial changes in microstructure during annealing.
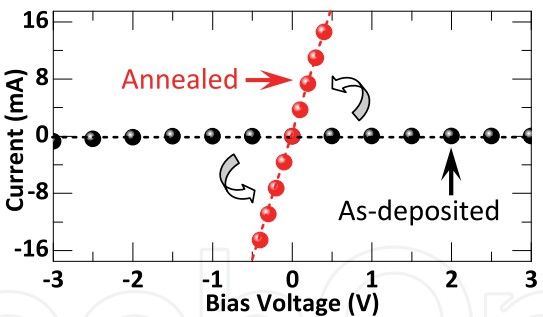
Fig. 1. Current-voltage properties of the TiAl contact system before and after thermal annealing at 1273 K for 2 min.

2.1.1 Formation of Ti_3SiC_2 compound on SiC

To determine the chemical composition of the TiAl contact systems, we performed XRD analyses, as shown in Fig. 2, where textural orientations of the detected matters are shown as well. As expected from the preparation process, one can see in Fig. 2(a) peaks of deposited metals, Ti and Al, and the (0001)-oriented SiC in the system before annealing. It is worthy of mentioning that the detected Ti has a much weaker intensity of diffraction peak than Al, which can be attributed to its lower concentration and smaller grains. On the other hand, the XRD spectrum alters significantly after annealing (Fig. 2(b)), as the original Ti and Al peaks disappear and there emerge new peaks, suggesting that chemical reactions occur.
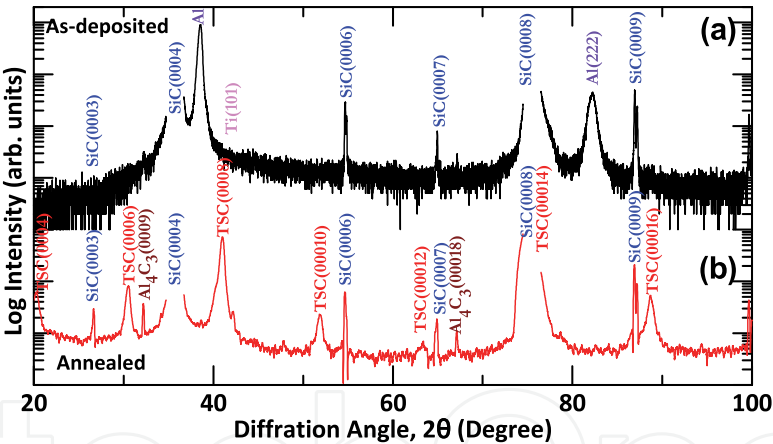
Fig. 2. XRD spectra of (a) as-deposited and (b) annealed TiAl contact systems. The TSC is an abbreviation of Ti_3SiC_2.

From Fig. 2(b), the reaction products are found to be dominated by ternary Ti_3SiC_2 with a strongly (0001)-oriented texture, as only the (000l) diffraction peaks are detected. In addition to the Ti_3SiC_2, binary Al_4C_3 is also present in the annealed specimen. However, its amount is very small because the intensities of its diffraction peaks are comparatively much weaker. The formation of these compounds at elevated temperature is also supported by the Ti-Al-SiC equilibrium phase diagram, which predicts that four phases, SiC, Al_4C_3, Ti_3SiC_2, and liquid, can coexist in an equilibrium state when the aforementioned composition of TiAl alloy is adopted. Furthermore, the XRD results agree well with the experimental reports (Johnson and Capano,2004), but deviate somewhat from those of Nakatsuka et al. (2002) showing that binary Al_3Ti is present as well. This slight difference is mainly because the intensity of Al_3Ti peak is so low that might be overlapped by the strong peaks of SiC and

Ti_3SiC_2. Finally, the SiC retains (0001)-oriented texture after annealing, thereby facilitating development of hetero-epitaxy between reaction products and substrates.

Figure 3 shows an isothermal section of the pseudo-ternary phase diagram of Al-Ti-SiC system at 1273 K (Viala et al., 1997) based on the experimental measurements of Al-Ti-Si-C quaternary system, where a grey region indicates the existence of binary AlSi-based liquid phases, and thick and fine lines indicates sub-solidus lines and tie-lines, respectively. It is noted that the liquidus line would lie at near the composition region of pure Al, as denoted by a symbol *L* in Fig. 3. Based on this phase diagram, the liquid phase is predicted to form when the concentration of Al is more than 75 at% in the Ti/Al contacts at 1273 K . In general, both the solutes and solvents have high diffusibility in liquid, the liquid phase has high reactivity to solid (substrate) and hence the reaction products are easily formed at elevated temperatures. Formation of the liquid is believed to play an important role in the TiAl-based contact by rapid thermal anneal process. Here, the effective average composition of the present reaction system, which react Ti-80%Al and SiC, can assume to be at the point *a* within region (i) in the diagram. In this region, four phases of SiC, Al_4C_3, Ti_3SiC_2 and liquid with a composition of Al-12%Si (which is a eutectic composition of Al-Si binary alloy) is predicted to maintain constant and coexist in equilibrium. This prediction is consistent with the XRD results obtained from samples annealed at 1273 K for 2 min (Fig. 2(b)), although a small amount of Al_3Ti and Al did not react completely with SiC and remained at this stage. Further annealing of the sample for longer time, for instance, 6 min, renders these unreacted Al_3Ti and Al disappear due to additional reaction to form the carbides (Ti_3SiC_2 and a small amount of Al_4C_3) and to the evaporation of Al-Si liquid phase with a high vapor pressure during annealing in ultra high vacuum. Hence, the average composition of the reaction system seems to shift toward Al-poor area (region (ii), as indicated by an arrow), and reach the point *b* after annealing. In the region (ii), three phases, SiC, Ti_3SiC_2 and Al-Si liquid with the Si concentrations varied from 12% (at the point *c*) to 19% (at the point *d*) are coexisted with their volume being constituted by an array of tie-lines. However, it is not straightforward to control the compounds formed by the rapid thermal annealing process because of occurrence of non-equilibrium phenomena such as evaporation of the liquid phases in this reaction system. This might be the reason why the TiAl-based contacts have been fabricated empirically with no definite designing guidelines.
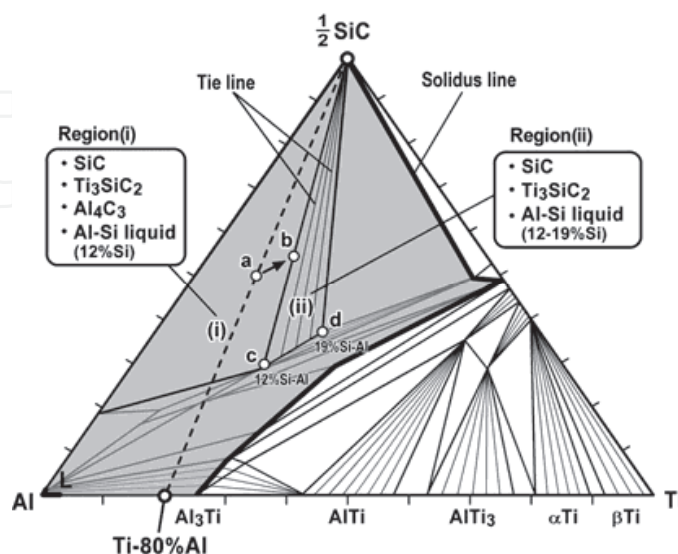

Fig. 3. Isothermal section of a pseudoternary phase diagram of Al-Ti-SiC system at 1273 K.

2.1.2 Growth and microstructure of Ti$_3$SiC$_2$ layers on SiC

To characterize the surface morphology of the TiAl contact layer after annealing, the SEM observation was employed. Figure 4 shows a plan-view SEM image from the TiAl contact layer after annealing at 1273 K. The surface is observed to have an uniformly scale-shaped contrast with hexagonal facets, although surface roughness after annealing is aggravated in comparison to that of the sample before annealing. Using a stylus surface profiler, the maximum typical roughness was measured to be about 1 μm. The surface facet planes are found to form parallel to <-2110> directions on the SiC(0001) substrate surface. The hillocks observed on the surface, which is due to formation of residual Al-based liquid droplet, is, however, absent for the samples annealed at temperatures lower than 1073 K. The surface morphology results from evaporation of the liquid phases with low melting points and high vapor pressures during annealing at high temperatures in ultra high vacuum.
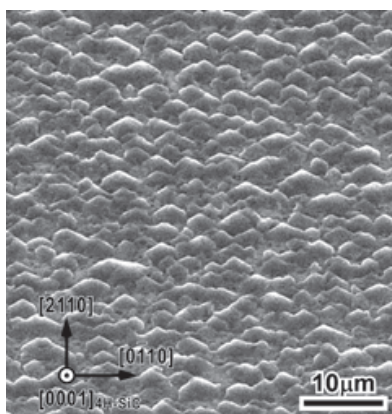
Fig. 4. A plan-view SEM image of the Ti/Al contact layers deposited on SiC after annealing at 1273 K.

Although the XRD can reveal detailed information on chemical composition of reaction products, it provides limited insight into matters concerning how the products distribute and contact the substrate. To observe the microstructure directly, we present in Fig. 5(a) a cross-sectional bright-field TEM image of a representative region in the annealed TiAl contact system. The incident electron beam is along [0-110] direction of the SiC, which is parallel to the tilting axis of the 8°-off SiC(0001) surface. As seen in this figure, the SiC surface is covered entirely by the plate-shaped Ti$_3$SiC$_2$ with thickness ranging from 30 nm to 300 nm. This universal cover means that no any other compounds contact directly the SiC surface, thereby ensuring an exclusive contact of Ti$_3$SiC$_2$ to SiC. Consequently, the SiC/Ti$_3$SiC$_2$ interface might play an essential role in the formation of Ohmic contact. In addition, this interface is observed to have a sawtooth-like facet structure and the Ti$_3$SiC$_2$ surface inclines by nearly 8° toward the substrate surface, suggesting that the SiC surface affects significantly morphology of formed Ti$_3$SiC$_2$.

To analyze the element species around interface, we further show in Fig. 5(b) the energy-dispersive X-ray spectroscopy (EDS) spectra for the interfacial SiC and Ti$_3$SiC$_2$ regions. The substrate is mainly composed of C and Si and the reaction products C, Si, and Ti, in accordance with chemical compositions of the substrate and the main reaction products, respectively. Unexpectedly, no Al peak is identified in either the interfacial SiC or Ti$_3$SiC$_2$ area, which seems to contravene the XRD analyses revealing that the Al$_4$C$_3$ compound is present in the annealed specimen. This discrepancy is mainly because the amount of Al$_4$C$_3$ is so small (Fig. 2(b)) that is hard to be detected by the EDS, or because Al might not distribute near the interface at all but around the Ti$_3$SiC$_2$ surface instead. Whatever the reason is, the Al should

not be the key to understanding the formation origin of Ohmic contact. That is, a large amount of Al diffuses into the SiC and introduces a heavily *p*-doped SiC, which result in narrower depletion area and thus more tunneling. As a matter of fact, this has also been suggested by analyzing interfacial chemical composition and local states, which shows that no additional Al segregates to interface, suggestive of a clean contact of Ti_3SiC_2 to SiC (Gao et al., 2007).
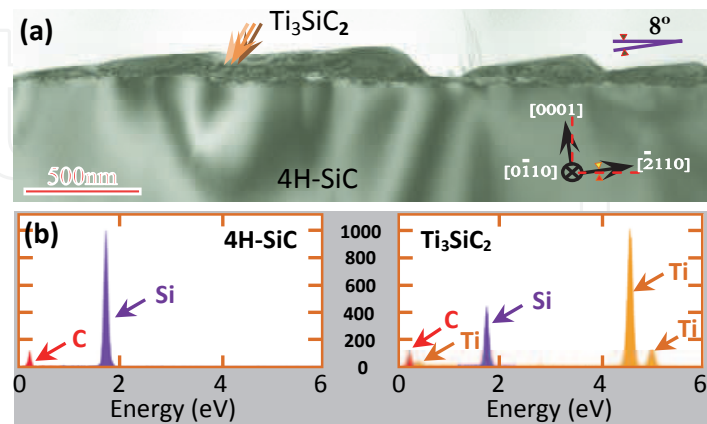

Fig. 5. (a) Cross-sectional bright-field TEM image of the annealed TiAl contact system showing exclusive reaction product of Ti_3SiC_2, and (b) EDS data obtained at the SiC and Ti_3SiC_2 region near to interface. The vertical axis in (b) denotes the counts (i.e., intensity).

Figure 6 shows a selected area diffraction pattern (SADP) at the contacts/SiC interface taken along the same electron-beam direction as in Fig. 5(a). A careful indexing of the pattern confirms again the plate-shaped layers as being ternary Ti_3SiC_2. The formed Ti_3SiC_2 layers are observed to have epitaxial orientation relationships, $(0001)Ti_3SiC_2//(0001)SiC$ and $[0\text{-}110]Ti_3SiC_2//[0\text{-}110]SiC$ with the SiC substrate, which agrees well with the XRD analyses demonstrating that both materials exhibit the (0001)-oriented textures. These orientation relationships are believed to be beneficial for forming a coherent and well matched interface between SiC and Ti_3SiC_2, since they both belong to the hexagonal space group with lattice constants of $a = 3.081$ Å and $c = 10.085$ Å for the SiC and $a = 3.068$ Å and $c = 17.669$ Å for the Ti_3SiC_2 (Harris, 1995).
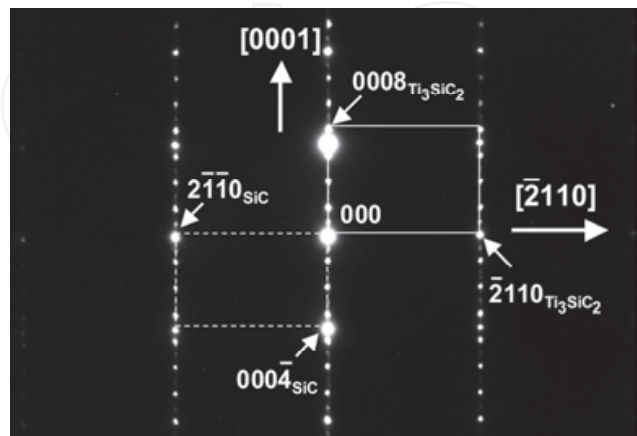

Fig. 6. Selected-area diffraction pattern obtained at the annealed contacts/SiC interface. The arrays of diffraction spots from the SiC and contacts are marked by dashed and solid lines, respectively.

In support of this idea, we present in Fig. 7 a cross-sectional HRTEM image of the SiC/Ti$_3$SiC$_2$ interface observed from the [11-20] direction. One can see clearly well arranged (000l)-oriented lattice fringes along the direction parallel to the interface in both the Ti$_3$SiC$_2$ layer and SiC substrate. The points at which the phase contrast is no longer periodic in either the Ti$_3$SiC$_2$ or SiC define the interfacial region. Evidently, the interface is atomically abrupt and coherent without any secondary phase layers, amorphous layers, contaminants, or transition regions, which confirms a clean and direct contact of the Ti$_3$SiC$_2$ with SiC on atomic scale. The interface has (0001)-oriented terraces and ledges, as marked by letters T_i (i = 1, 2, 3, 4) and L_j (j = 1, 2, 3) in Fig. 7, respectively. The morphology of the terraces is observed to be atomically flat and abrupt as well. On the other hand, the ledge heights are found to be defined well as n × (a half unit cell height of 4H-SiC: 0.5 nm), where n represents the integer, e.g., n = 11 for L_1, n = 2 for L_2, and n = 1 for L_3. This unique interface morphology is caused by the chemical reaction of TiAl and SiC, and anisotropic lateral growth of the epitaxial Ti$_3$SiC$_2$ layers along the directions parallel to SiC(0001), as indicated by arrows in Fig. 7. In addition, no misfit dislocations are clearly visible at interface in present HRTEM micrograph and further examination of other interfacial regions demonstrates that the density of misfit dislocations is extremely low in this system. This can be explained from the small lattice mismatch between the two materials (less than 0.5%). Unfortunately, it remains unclear from this figure how the two materials atomically bond together at interface, which is very important because the bonding nature is well known to be able to affect the physical properties of interfacial systems significantly.
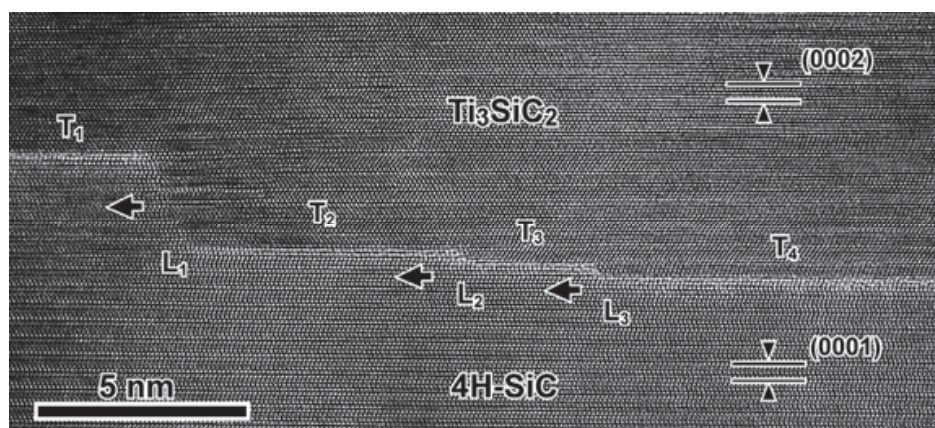

Fig. 7. A cross-sectional HRTEM micrograph of the interface between the Ti$_3$SiC$_2$ layer and the 4H-SiC substrate, which is taken along the SiC [-2110] zone axis.

2.1.3 Interface atomic-scale structures

Figure 8 shows a typical HAADF image of the SiC/Ti$_3$SiC$_2$ interface. A simple looking at this figure confirms a clean and atomically sharp contact between the two materials, which means a successful growth of the epitaxially Ti$_3$SiC$_2$ on SiC. Brighter spots in the image represent atomic columns of Ti, while the comparatively darker ones are Si, since the intensity of an atomic column in the STEM, to good approximation, is directly proportional to the square of atomic number (Z) (Pennycook & Boatner, 1988). Not surprisingly, due to small atomic number of C, its columns are not scattered strongly enough to be visualized, thereby making the image incomplete. Further complementing of this image so as to relate the atomic structure to property requires the first-principles calculations.
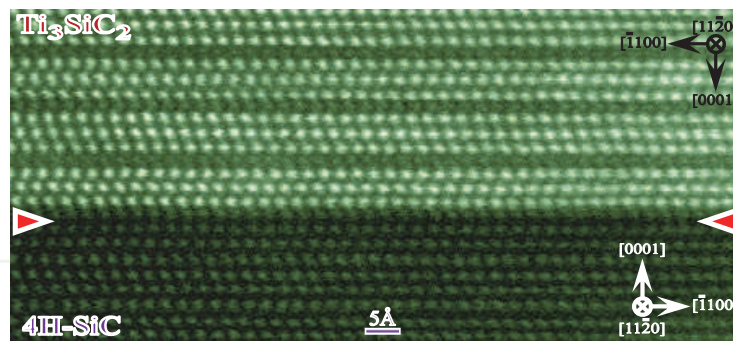
Fig. 8. A typical HAADF-STEM image of the SiC/Ti$_3$SiC$_2$ interface in the annealed TiAl contact system observed from the [11-20] direction. The position of interface is indicated by two arrows

To see the interface atomic-scale structure clearer, we magnify the cross-sectional HAADF image of the SiC/Ti$_3$SiC$_2$ interface in Fig. 9(a) and further filter it to reduce noise (Fig. 9(b)). The interface location is indicated by a horizontal line, which is determined based on the arrangement of atomic columns in bulk SiC and Ti$_3$SiC$_2$. The Si-terminated Ti$_3$SiC$_2$ is observed intuitively to make a direct contact with the Si-terminated SiC substrate with the interfacial Si atoms of Ti$_3$SiC$_2$ sitting above hollow sites of the interfacial Si plane of SiC. However, as we will see in the upcoming simulations, this interpretation is premature in that it neglects a possibility, namely, the unseen C might be trapped at interface. Another interesting feature in this figure is that no Al columns are detected surrounding interface, which eliminates the possibility of additional p-doping via Al diffusion into the top few SiC layers. Since there are also no pits, spikes, or dislocations which might act as pathways for current transport, we conclude that the clean and coherent SiC/Ti$_3$SiC$_2$ interface should be critical for the Ohmic contact formation. The ensuing question is how this interface lowers the Schottky barrier, which is rather difficult to investigate by experiment alone but can be suggested by calculations.
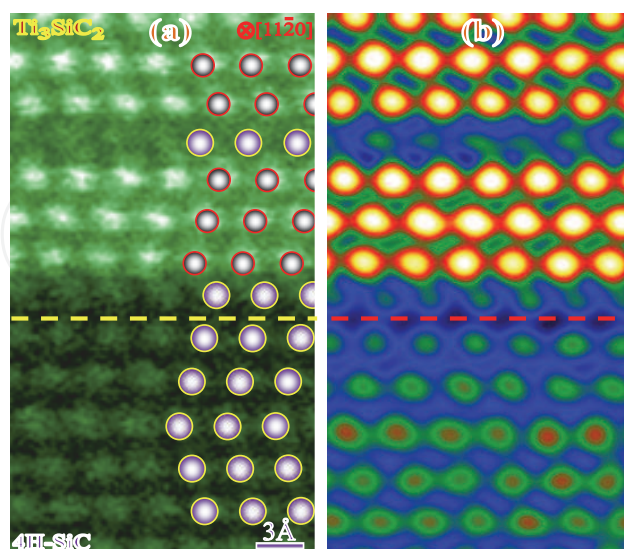

Fig. 9. A(a) Magnified HAADF image of the SiC/Ti$_3$SiC$_2$ interface. An overlay is shown as well for easy reference. The bigger balls denote Si and the smaller ones Ti. (b) The same image as in (a) but has been low-pass filtered to reduce the noise.

3. Atomistic modelling of the functional interface

Calculations of electronic structure and total energy were carried out using the Vienna *ab initio* simulation package (VASP) within the framework of density- functional theory (DFT) (Kresse & Hafner, 1993). The projector augmented wave (PAW) method was used for electron-ion interactions and the generalized gradient approximation (GGA) of Perdew and co-worker (PW91) was employed to describe the exchange-correlation functional. The single-particle Kohn-Sham wave function was expanded using the plane waves with different cutoff energies depending on calculated systems of either bulk or slab. Sampling of irreducible wedge of Brillion zone was performed with a regular Monkhorst-Pack grid of special *k* points, and electronic occupancies were determined according to a Methfessel-Paxton scheme with an energy smearing of 0.2 eV. All atoms were fully relaxed using the conjugate gradient (CG) algorithm until the magnitude of the Hellmann-Feynman force on each atom was converged to less than 0.05 eV/Å, yielding optimized structures.

The electron transport properties of the above systems were explored with the fully self-consistent nonequilibrium Green's function method implemented in Atomistix ToolKit (ATK) code. This method has been applied to many systems successfully. The local density approximation (LDA) and the Troullier-Martins nonlocal pseudopotential were adopted, and the valence electrons were expanded in a numerical atomic-orbital basis set of single zeta plus polarization (SZP). Trial calculations exhibit similar results by using double zeta plus polarization (DZP) basis sets for all atoms, thereby validating the use of SZP. Only Γ-point was employed in the *k*-point sampling in the surface Brillouin zone. A cutoff of 100 Ry for solving Poissons equation and various integrals is utilized to present charge density and a rather large k-point value, 200, is chosen for accurately describing electronic structure along transport direction.

3.1 Bulk and surface calculations
3.1.1 Bulk properties

We first assess accuracy of the computational methods by performing a series of bulk calculations. It is known that the 4H-SiC, one of the most common SiC polymorphs, belongs to hexagonal $P6_3mc$ space group with a = 3.081Å and c = 10.085Å. A unit cell of SiC consists of four Si-C bilayers with a total of 8 atoms. The Ti_3SiC_2 also has a hexagonal crystal structure but within the $P6_3mmc$ space group (a = 3.068Å and c = 17.669Å). The atomic positions of Ti correspond to the 2*a*, Si to the 2*b*, and C to the 4*f* Wyckoff sites of the space group and the phase is composed of a layered structure with a double Ti-C block, each made up of two edge-sharing CTi6 octahedra. Note that the Ti atoms of Ti_3SiC_2 occupy two types of structurally nonequivalent positions: one (Ti1, two per unit cell) has C atoms as nearest neighbors, while the other (Ti2, four per unit cell) has Si atoms (see Fig. 13(a)). The optimum lattice constants of bulk 4H-SiC calculated using the above parameters are a = 3.095Å and c = 10.131Å, 100.5% of the experimental value, while those of bulk Ti_3SiC_2 are a = 3.076Å and c = 17.713Å, 100.25% of the experimental one (Harris, 1995).

Figure 10(a) shows calculated band structure of 4H-SiC along the high-symmetry lines. The top of occupied valence band (VB) is located at Γ point and the bottom of conduction band (CB) is at M point, causing the SiC to be an indirect gap semiconductor. The calculated energy band gap is 2.25 eV, which is smaller than the experimental value of 3.26 eV, but close to the calculated value of 2.18 eV (Käckell et al., 1994) and 2.43 eV (Ching et al., 2006). Deviation from the experimental value is attributed to the well-known drawback of the DFT

which tends to underestimate band gap. The band gap in Fig. 10(a) can also be seen from the total DOS shown in Fig. 11(a). Besides this gap around the Fermi level (E_F), there is also a gap of more than 1 eV located at about -10 eV below the E_F, dividing the entire VB into two parts. The lower part of the VB originates mainly from the bonding between the s states of the Si and C, while the upper one is dominated by p orbitals of Si and C in a form of sp^3 hybridization. The CB part, however, shows a continuum state throughout the whole region, which is reflected from interweaving lines above E_F (Fig. 10(a)).
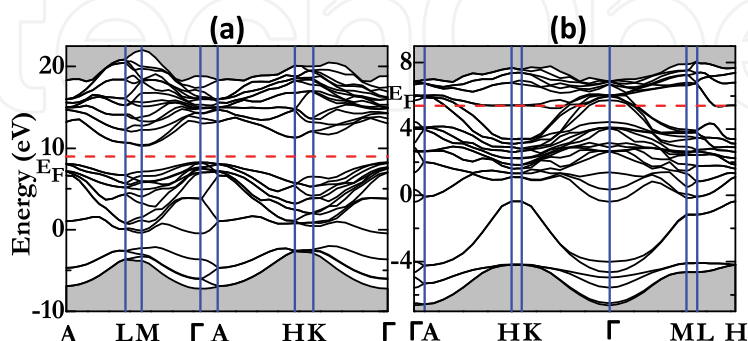
Fig. 10. Energy band structure of (a) 4H-SiC and (b) Ti$_3$SiC$_2$ along the major symmetric directions. The dotted lines in red denote the Fermi level (E_F).

In contrast, Ti$_3$SiC$_2$ exhibits clearly a metallic nature with bands crossing the E_F, as shown in Fig. 10(b), thereby resulting in a peak in the total DOS at E_F in Fig. 11(b). It is worth noting that the presence of the band at E_F is caused by the energetic overlap of Ti d states with the gap levels of SiC (Fig. 11(b)), not an artifact due to the DFT underestimation of band gap. This metallic character is in agreement with reported experimental results and other theoretical studies. From Fig. 10(b), one can see that the VB of Ti$_3$SiC$_2$ is also separated into two parts at approximately 5.7 eV below E_F, the lower part of which is composed of metalloid states having a typical s symmetry while the upper part of which consists of complex bands. It is also clear from Fig. 11(b) that these complicated states just below E_F are dominated by strongly hybridized bonding states containing mainly p orbitals of both Si and C and d orbitals of Ti. The contribution to the CB, however, comes predominantly from antibonding d states of Ti, as shown in the PDOS of Ti in Fig. 11(b). The magnitude of DOS at E_F is equal to 3.5 states/eV per unit cell, originating considerably from Ti d states together with a slight contribution from Si p states
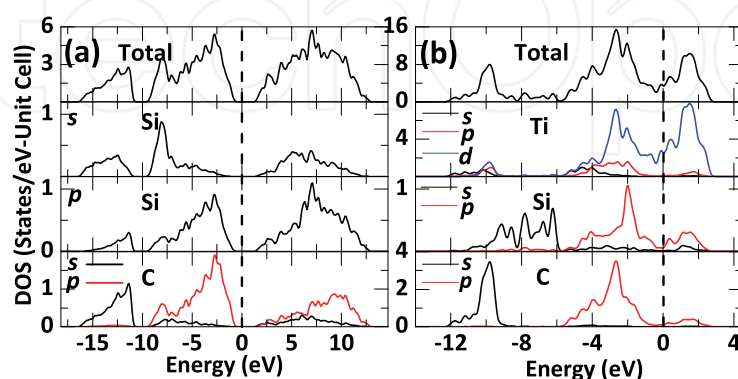

Fig. 11. Calculated total and partial densities of states (PDOS) for (a) 4H-SiC and (b) Ti$_3$SiC$_2$. The Fermi level is set to zero and marked by a vertical dash line. The PDOS of Ti encompasses those of two types of nonequivalent Ti positions, Ti1 and Ti2.

3.1.2 Surface properties

To simulate a bulklike interface, it is essential to ensure that the two sides of the interface slabs used in calculations are thick enough to exhibit a bulklike interior because properties of a thin film may differ significantly from those of the bulk. To determine the minimum layer necessary for a bulklike slab, we first performed calculations on the convergence of surface energy with respect to slab thickness and then considered an additional series of surface relaxations as a function of slab layers. The surface energy of Ti$_3$SiC$_2$, σ_T, under pressure P and temperature T can be expressed as follows:

$$\sigma_T = \frac{1}{2A}(E_{slab}^{total} - N_{Ti}\mu_{Ti} - N_{Si}\mu_{Si} - N_C\mu_C - PV - TS) \qquad (2)$$

where, E_{slab}^{total} denotes total energy of a relaxed and isolated slab, and μ_X, N_X, A represent chemical potential of X (X = Ti, Si, C), number of X atoms in the slab, and surface area, respectively. For Eq. (2), the TS term can be deleted at 0 K and meanwhile, the PV term is negligible for low pressure because we are considering a condensed matter system. Further, chemical potential of condensed phase of Ti$_3$SiC$_2$, $\mu_{Ti3SiC2}$, can be given by a sum of three terms representing chemical potential of each species within the crystal:

$$\mu_{Ti_3SiC_2} = 3\mu_{Ti} + \mu_{Si} + 2\mu_C. \qquad (3)$$

Since the total chemical potential of surface system, $\mu_{Ti3SiC2}$, is in equilibrium with that of its bulk, $E_{Ti_3SiC_2}^{bulk}$, we thus have

$$\mu_{Ti_3SiC_2} = E_{Ti_3SiC_2}^{bulk}. \qquad (4)$$

Replacing Eq. (4) with Eqs. (2) and (3), one can eliminate the $\mu_{Ti3SiC2}$ and μ_C variables in the surface energy of Ti$_3$SiC$_2$, σ_T, and obtain

$$\sigma_T = \frac{1}{2A}[E_{slab}^{total} - \frac{1}{2}N_C E_{Ti_3SiC_2}^{bulk} - \mu_{Ti}(N_{Ti} - \frac{3}{2}N_C) - \mu_{Si}(N_{Si} - \frac{1}{2}N_C)]. \qquad (5)$$

When the chemical potentials of the Ti and Si equal total energies of the hexagonal close-packed bulk Ti, E_{Ti}^{bulk}, and fcc bulk Si, E_{Si}^{bulk}, respectively, the Eq. (5) can be redefined as

$$\sigma_T^0 = \frac{1}{2A}[E_{slab}^{total} - \frac{1}{2}N_C E_{Ti_3SiC_2}^{bulk} - E_{Ti}^{bulk}(N_{Ti} - \frac{3}{2}N_C) - E_{Si}^{bulk}(N_{Si} - \frac{1}{2}N_C)]. \qquad (6)$$

Similarly, the surface energy of the SiC, σ_S^0, can be given by the following equation under the condition that chemical potential of Si is equal to its bulk total energy.

$$\sigma_S^0 = \frac{1}{2A}[E_{slab}^{total} - N_C E_{SiC}^{bulk} - E_{Si}^{bulk}(N_{Si} - N_C)] \qquad (7)$$

Experimentally, the SiC(0001) plane was observed to be a favorable substrate surface that allows epitaxial growth of Ti$_3$SiC$_2$ with also a (0001)-oriented face. Four types of SiC terminations within the (0001) surface have been investigated, as shown in Fig. 12(b)-(e). In view of the unequal atom species at two sides of a stoichiometric slab, a non-stoichiometric

slab with identical surface layer must be used to extract surface energy of a particular termination. Initial convergence tests show that 10 Å of vacuum, 8×8×1 irreducible *k* points and a cut-off energy of 400 eV ensure total-energy convergence to less than 1 meV/atom. All of the atoms were fully relaxed until magnitude of force on every atom is smaller than 0.05 eV/Å. With these parameters, we first calculated surface energies of Si-terminated SiC with slabs varying from 5 to 17 layers using Eq. (7) and found that a 9-layer slab is enough to exhibit good convergence of surface energy. Next, we examined relaxation of the SiC(0001) surface slabs so as to ensure that they are reasonably converged with respect to slab layers. The SiC(0001) surface shows a low degree of interlayer relaxations with maximum of less than 3% of the bulk spacing for 9 or more layers thick.
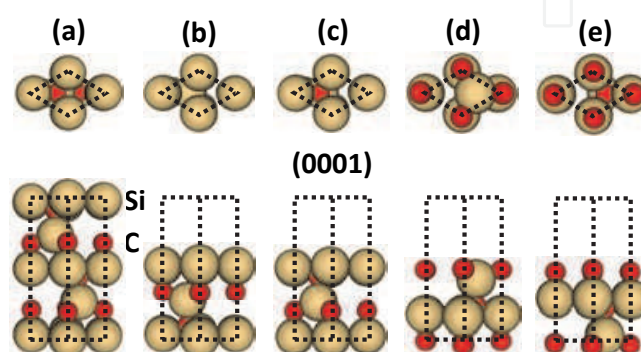

Fig. 12. Schematic plot of 4H-SiC: (a) bulk, (b) Si1, (c) Si2, (d) C1, and (e) C2 terminations. The upper part shows the top view, while the lower one shows the side view. Only the top five of nine symmetric layers are presented for each termination.
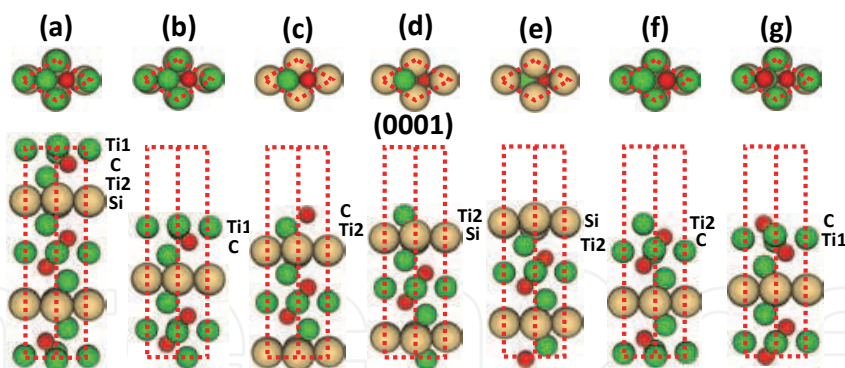

Fig. 13. Top (upper part) and side (lower part) view of Ti$_3$SiC$_2$: (a) bulk, (b) Ti1(C), (c) C(Ti2), (d) Ti2(Si), (e) Si(Ti2), (f) Ti2(C), and (g) C(Ti1) termination. Only the top nine layers of each symmetric slab are presented for each termination.

The Ti$_3$SiC$_2$(0001) surface can be terminated with C, Si, any of two types of Ti (Ti1 and Ti2), or their combinations, yielding a total of six possible surface geometries. Figure 13(b)-(g) shows the six terminations: Ti1(C), C(Ti2), Ti2(Si), Si(Ti2), Ti2(C), and C(Ti1), where the letter in the brackets denotes sub-surface atom. The surface energies of Ti1(C) termination calculated using Eq. (6) is found to converge well to 0.84 J/m² by a 13-layer-thick slab. Further, interlayer relaxations also show a good convergence for slabs having 13 layers or more. Contrast to the small relaxation presented in the SiC(0001), here there is a larger interlayer relaxation, especially for the first layer, which attenuates rapidly within two

surface layers. Lastly, we also calculated the surface energies of the remaining terminations in Fig. 13(c)-(g) to be 4.10, 0.64, 1.12, 1.56 and 5.60 J/m^2, respectively. In summary, we have calculated the bulk and surface properties for SiC and Ti_3SiC_2 and shown that these values are consistent with existing experimental and theoretical data, thereby offering not only detailed information but also a verification of applicability of the method and model for further interface investigation.

3.1.3 Interface construction and calculation process

A total of 96 possible candidate interface models have been considered within the above orientation relations, including four SiC terminations (Fig. 12(b)-(e)), six Ti_3SiC_2 terminations (Figs. 13(b)-(g)), and four different stacking sequences for each combination of SiC and Ti_3SiC_2 terminations. In the four stacking sequences, the interfacial Ti (C or Si) of Ti_3SiC_2 are located (i) on top (OT) of the surface atoms of SiC, (ii) at the center of the rhombic (RC) unit cell, (iii) above second-layer (SL) atoms of SiC, and (iv) above hollow sites (HS) of SiC, as shown in Fig. 14. These stacking sequences are of high symmetry and thus more likely to correspond to total-energy extrema. According to the surface calculations, our interface models are composed of a nine-layer symmetric SiC(0001) slab (bottom of Figs. 12(b)-(e)) connected to a symmetric Ti_3SiC_2(0001) slab (top of Fig. 13(b)-(g)) of at least 13 atomic layers. A 10 Å area of vacuum was added so as to minimize the coupling perpendicular to the interface. To form coherent interfaces, in-plane lattice constants of the Ti_3SiC_2 slab are expanded by 0.63% to match those of the harder SiC slab, while out-of-plane ones are fixed to their GGA optimized bulk values. Two steps were adopted to estimate W_{ad}. First, total energies were calculated for various separations as two slabs were brought increasingly closer from a large initial separation. As a consequence, the total energy is found to behave likes a parabola, passing through a minimum at the equilibrium separation. The unrelaxed W_{ad} was obtained by computing the energy difference between the interface at equilibrium separation and the unrelaxed isolated slabs. Next, full relaxation of each isolated slab and interface slab was allowed, which yielded an estimate of relaxed W_{ad}.
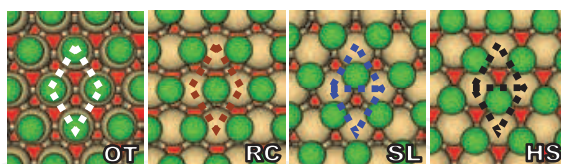

Fig. 14. Schematic plots of four different stacking sequences. Only the Ti layer of Ti_3SiC_2 proximal to the interface is presented for clarity. The smallest red spheres, intermediate green spheres, and largest golden spheres represent C, Ti, and Si atoms, respectively. The dotted parallelogram outlines the SiC rhombic unit cell projected along the [0001] direction.

3.1.4 Determination of interface atomic structure

To clarify the mechanism theoretically, we first determined atomic structure of SiC/Ti_3SiC_2 interface via complementing the acquired HAADF image (Fig. 9). In light of bulk structures of 4H-SiC and Ti_3SiC_2, the aforementioned orientation relations, and the relative stacking order of Ti and Si, the observed image in Fig. 9 can be intuitively fitted by two models among all the 96 candidates: SiSi and SiCSi model (Fig. 15). In the SiSi model, the interfacial Si atoms of Ti_3SiC_2 sit above the hollow sites of interfacial Si plane of SiC, where the optimal distance between interfacial Si-Si planes (denoted as $d1$ in Fig. 15(a)) and that between

interfacial Si-Si atoms projected onto paper plane (denoted as $d2$ in Fig. 15(a)) are calculated to be 2.13 and 2.53 Å (Table I), respectively. These distances, however, deviate severely from their average experimental values, 2.5 and 2.8 Å, which are obtained by characterizing quantitatively the HAADF image (Fig. 9(a)). In addition, an examination of interface stability by calculating the W_{ad} indicates that the SiSi model is not favored at all (1.62 J/m²). It is even less stable than the model with interfacial Si of Ti_3SiC_2 resting straight atop the interfacial Si of SiC (2.58 J/m²), which contravenes again the observed image. Why does the less preferred interface predicted by our simulations emerge in experiments? It is worth noting that many other regions have been examined using the STEM but no other possibility is observed.
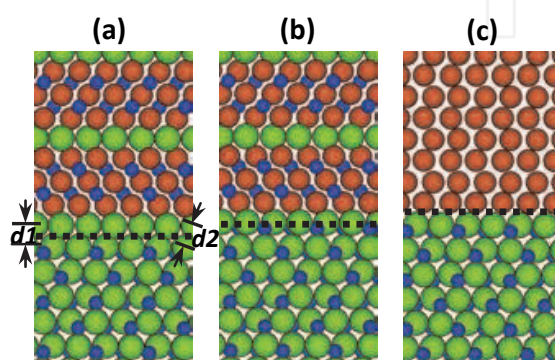

Fig. 15. Relaxed SiC(0001)/Ti₃SiC₂(0001) interface models (a) without interfacial C atoms (SiSi) and (b) with interfacial C atoms (SiCSi). (c) Optimized SiC(0001)/Ti(0001) interface model. The distance between interfacial Si-Si layers (Si-Ti layers for (c)) is represented by $d1$ and that between interfacial Si-Si atoms (Si-Ti atoms for (c)) projected onto the paper plane by $d2$. The interfaces are represented by dotted lines.

Could these pronounced discrepancies between results of experiment and calculation be ascribed to computational inaccuracies? Since the calculation parameters described above are verified to be sufficient to ensure a total energy precision of better than 1 meV/atom, one might be concerned that another numerical inaccuracy arises from size effect of the used slabs. However, we found this inaccuracy to be within 0.1 J/m² via enlarging the slabs along the interface, so that it does not affect our simulated W_{ad}. In addition, convergence tests show that the used slab thickness yields surface energy convergence to smaller than 0.02 J/m². Furthermore, the used GGA functional was tested to evaluate bulk lattice constants and distances between atoms within an error of less than 0.5%. Finally, there is a small lattice mismatch of 0.63% at interface, which can be damped out by structural optimization. Moreover, Wang et al. have reported that a lattice mismatch as large as 3.9% at an interface varies the W_{ad} only by less than 5% (Wang et al., 2002). Therefore, it seems that the discrepancies should not simply be attributed to the computational error.

To resolve these paradoxes, we noticed that a possibility might be ignored, that is, the unseen C might be trapped at interface, altering the local environment there. To test this hypothesis, the other SiCSi model was established by introducing C into the interfacial layer from the consideration of crystal extension and stacking sequences. The calculated W_{ad} of this SiCSi model is listed in Table I, where the interface is strengthened substantially after the incorporation of C. Investigation into its fully optimized atomic configuration (Fig. 15(b)) reveals that the incorporation of C does not induce significant interface reconstruction. Namely, the two Si layers proximal to the interface maintain the stacking

seen in Fig. 15(a), thus matching the HAADF image geometrically. Quantitatively, the $d1$ and $d2$ distances are now 2.53 Å and 2.81 Å (see Table I), respectively, very close to the obtained experimental values. Therefore, the introduction of interfacial C monolayer resolves the inconsistencies between simulations and experiments. Finally, we superimpose the calculation-inferred atomic structure of SiCSi interface (Fig. 15(b)) onto the HAADF image (Fig. 9(a)) and find that they match very well.

	SiSi	SiCSi	SiTi
W_{ad} (J/m²)	1.62	6.81	2.06
$d1$ (Å)	2.13	2.31	2.36
$d2$ (Å)	2.53	2.81	2.97
SBH (eV)	1.05	0.60	1.10

Table 1. Relaxed W_{ad} (J/m²), optimal interfacial distances $d1$ and $d2$ (Å), and calculated p-type Schottky barrier heights (SBH) (eV) for the SiC/Ti$_3$SiC$_2$ interfaces without (SiSi) and with interfacial C (SiCSi), and for the SiC/Ti interface (SiTi). Refer to Fig. 15 for their schematic configurations

3.1.5 Schottky barrier height
To further examine whether the determined interface has a less Schottky character, we calculated p-type Schottky barrier height (SBH), an important quantity in analyzing electric properties of a metal/semiconductor contact interface. The p-type SBH is calculated from the difference between the E_F of interface supercell and the valence-band top of bulk SiC region. It should be noted that due to the well-known problem of discontinuity in the exchange-correlation potential across heterointerface, an exact quantitative estimation of SBH is unlikely. However, the qualitative comparisons between the calculated SBHs for different interface configurations should be reliable. The p-type SBHs for the SiC/Ti$_3$SiC$_2$ interfaces with and without interfacial C are listed in Table I, where the SBH for the SiTi interface (Fig. 15(c)) is listed as well for comparison. From this Table, one can see that the SiCSi interface shows the lowest SBH, meaning that it is of the least Schottky nature.

3.1.6 Electronic structure and chemical bonding
To shed light on origin of decrease in SBH and junction strengthening in the SiCSi interface, several analytic approaches were applied to characterize in detail interfacial electronic states and bonding nature. First, we calculated planar-averaged charge density and its difference along the interface normal. The density difference is evaluated by subtracting the sum of charge density of isolated SiC and Ti$_3$SiC$_2$ slabs from the total interface charge density. As seen in Fig. 16(a), after introducing the C, an interfacial Si-C pair is generated in the SiCSi case in a way similar to the pair in bulk SiC. As a result of the formation of the pair, there is a dramatic accumulation of charge within the interfacial region, in contrast to what is seen in either the SiSi or SiTi interface (Fig. 16(a)). This indicates that the covalent bonding is strengthened for the SiCSi. Evidently, the large degree of charge accumulation at interface is at the expense of depletion of charge in the sub-interfacial layers between Si and Ti, suggestive of weakened bonding between them. This is a short-range effect, however, since the charge density returns to its bulk value by the second layer. From Fig. 16(b), we note that the planar-averaged density difference for the SiCSi most prominently deviates from zero around the interface, reflecting the most significant charge transfer between SiC and Ti$_3$SiC$_2$ slabs. In addition, charge is

observed to be depleted noticeably in both the sub-interfacial SiC and Ti_3SiC_2 region for the SiCSi, suggesting that the atoms second nearest to the interface contribute to the interfacial bonding. These missing charges, to a large extent, make their way onto the more electronegative C ions, indicative of formation of ionic bonding.
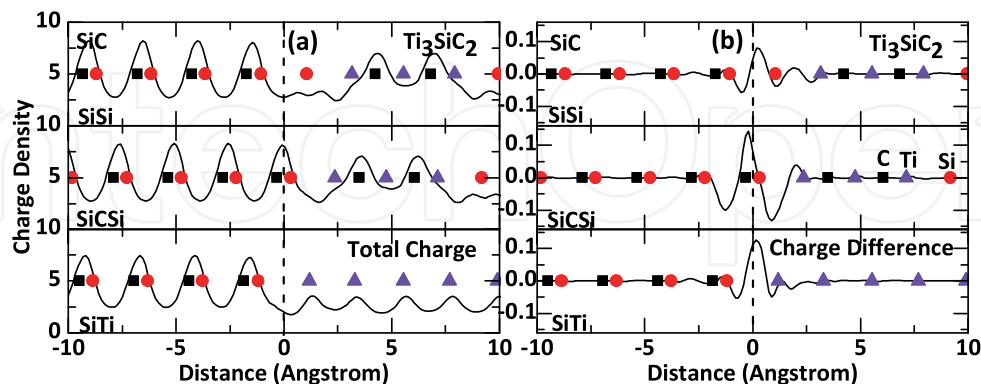

Fig. 16. Planar-averaged (a) total charge density and (b) charge-density difference for the relaxed SiSi, SiCSi, and SiTi interfaces along [0001] direction. The solid rectangles, circles, and triangles give the locations of C, Si, and Ti atoms, respectively. The interface position is set to zero and indicated by a vertical line

Figure 17 presents DOS projected on selected atomic layers of the SiCSi interface in order to gain insight into electronic states. Overall PDOS shape of interfacial Si of Ti_3SiC_2 resembles to some extent that of a Si layer deeper in SiC but deviates remarkably from that of a Si layer deeper in Ti_3SiC_2 (7th layer), which can be reflected from the formation of Si-C pair. Moreover, this suggests that the substrate has a fundamental effect on the interface electronically. A key feature in this figure is that a strong interaction is observed between the sub-interfacial Ti d and Si p states below E_F, which continues well into the SiC surface, inducing noticeable gap states in the interfacial C at E_F. This means that the interfacial C layer, the first monolayer on the substrate, is metallized, indicative of possible electric conductivity. In fact, the gap states can extend as far as they can into deeper layers of SiC, as there appear weak but visible peaks at E_F in the PDOSs of the 2nd and 3rd layers of SiC. Consequently, a local weak metallicity might occur in top few layers of the semiconductor surface, which could enable current flow through the SiC. Apart from the peaks in SiC, all of the Ti_3SiC_2 layers exhibit notable peaks at E_F, which can be attributed to the large degree of overlap between Ti d and C (Si) p states. Finally, we note significant hybridization between the interfacial C sp and Si sp states, suggestive of covalent bonding at interface.

To identify the bonding type directly, we further show contour plots of charge densities (Fig. 18) and their differences (Fig. 19) along the (11-20) plane for the optimized SiSi, SiCSi and SiTi interfaces. From Fig. 18, we notice first that the bonding interaction between the interfacial Si and C for the SiCSi interface is remarkably similar to the Si-C interaction deeper into SiC: the majority of charge is localized on C with humps directed towards their adjacent Si. We thus conclude that the interfacial bonding for the SiCSi is of mixed covalent-ionic nature. The interfacial bonds for the SiSi interface, however, exhibit covalent character with a small amount of charge accumulated within the interfacial region (Fig. 18(a)), in consistence with our analyses on planar-averaged density-difference (Fig. 16). As for the SiTi, the charge distribution of interfacial Ti is almost identical to that of Ti away from interface, having a character of weakly but broadly distributed charge density. This indicates that the interfacial bonds for the SiTi take on weakly metallic nature, yet maintain a small degree of covalency. The covalency can be

further confirmed from the density-difference plot (Fig. 19(c)) displaying charge accumulation along the interfacial Si-Ti bonds. The amount of charge accumulated on the Si-Ti bonds is larger than that on the interfacial Si-Si bonds of SiSi (Fig. 19(a)) but far less significant than that on the interfacial Si-C bonds of SiCSi (Fig. 19(b)). This heaviest charge accumulation along the interfacial Si-C bonds, together with the mixed covalent-ionic character at the SiCSi interface, explains the largest W_{ad} associated with the SiCSi interface (Table I). Finally, we note from both figures that charge variations due to the interface are screened rapidly with distance from interface, suggesting that the interface effect is confined to within a short range, in agreement with the previous analyses on PDOS and planar-averaged charge.
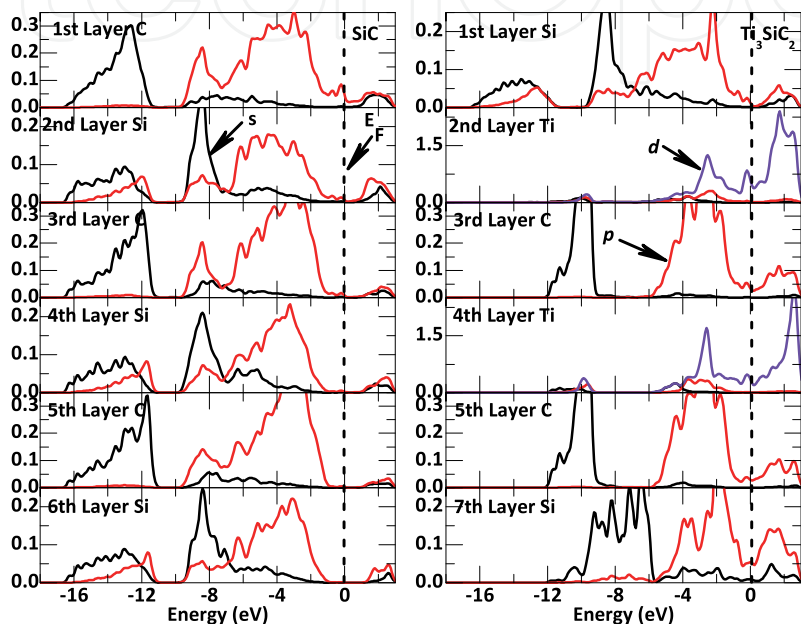
Fig. 17. PDOS (states/eV atom) projected on the atomic layers close to the relaxed SiCSi interface. The left panel shows PDOSs of SiC layers and the right one those of Ti$_3$SiC$_2$ layers. The first layer is the atomic layer proximal to interface. The E_F is set to zero.
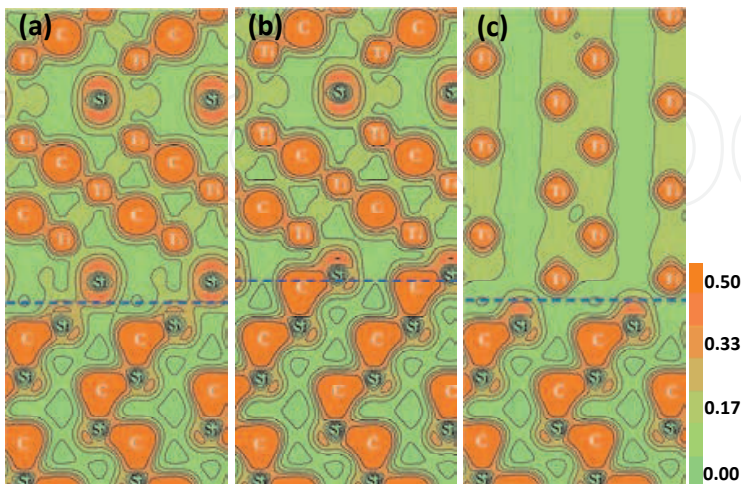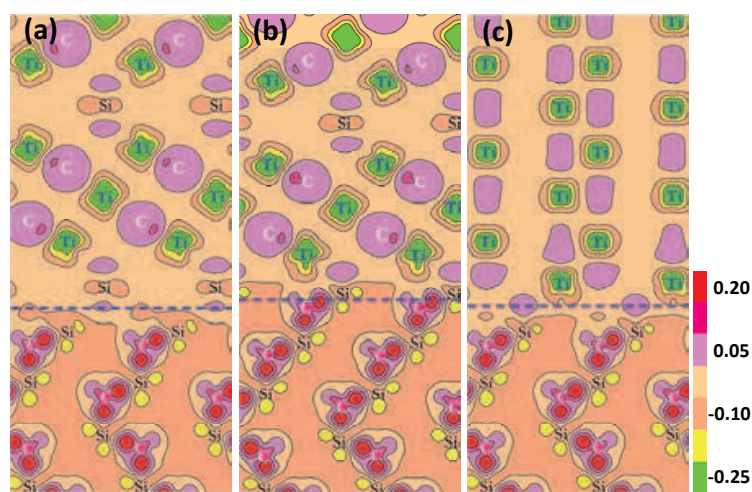

Fig. 18. Contour plots of charge densities for (a) SiSi, (b) SiCSi, and (c) SiTi interfaces taken along the (11-20) plane. The interface is represented by a horizontal line and the atoms that intersect the contour plane are labeled.

To further explain the decrease in SBH for the SiCSi, we plotted the variation of electrostatic potential along the interface normal in Fig. 20, where potential changes for the SiSi and SiTi interfaces are shown as well. As a result of the large interface dipole generated by the considerable charge transfer (Fig. 16(b)) and the partial ionicity (Fig. 18(b)), the electrostatic potential of interfacial Si in the SiCSi is lowered significantly relative to its adjacent SiC region (Fig. 20(b)), which consequently enables the reduction of SBH. This is contrary to the SiSi (Fig. 20(a)) and SiTi (Fig. 20(c)) cases, as their electrostatic potentials are high at interface. These high potentials indicate that electrons might be transferred from the SiC surface to the interface, resulting in electron depletion on substrate surface. Moreover, we note in Fig. 20 that electrostatic potential for Si atoms is always lower than that for the Ti or C atoms, which explains the lower electron density of Si shown in the charge-distribution plot (Fig. 18).

Fig. 19. Contour plots of charge-density differences for (a) SiSi, (b) SiCSi, and (c) SiTi interfaces taken along the (11-20) plane. The difference of charge density presents redistribution of charge in the interface relative to its isolated system.
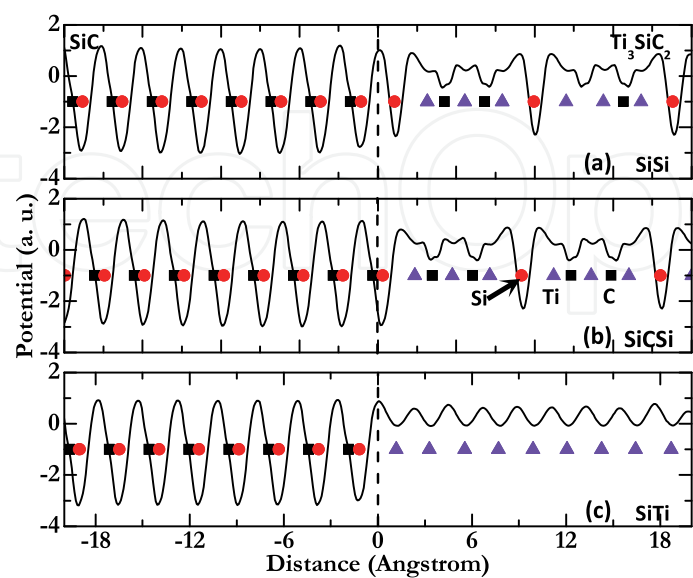

Fig. 20. Electrostatic potential as a function of distance from interface along the [0001] direction for (a) SiSi, (b) SiCSi, and (c) SiTi interfaces. Interface position is set to zero.

3.1.7 Electron density near fermi level

Although the charge-distribution analysis can reveal valuable information on interfacial bonding, it provides restrained insight into how electrons distribute around E_F, which matters because density around E_F directly determines the current transmission. Figure 21 illustrates an electron-density isosurface and its slice along the (11-20) plane for the optimized SiCSi interface around E_F. From Fig. 21(a), one can see that charges surrounding interfacial Si are connected and broadly distributed in a sheet-like fashion, which suggests a possible electrical conductivity through this region. In addition, there also appear heavily accumulated electrons within the interfacial area, which are connected along the interface and extended as far as several atomic layers into the SiC. These characters can also be confirmed from the slice plot in Fig. 21(b), meaning that current might flow over the top few atomic layers of semiconductor, thereby causing Ohmic property. As expected, the electron density at E_F is extremely high for the Ti_3SiC_2 (i.e., sea of electrons) but becomes nil for the SiC layers away from interface (Fig. 21(b)), which can be understood from their intrinsic metallic and semiconducting nature.

3.1.8 Quantum electron transport property

To examine electrical conductivity and gain insight into how the interface influences current transport, we devised a two-probe system, $Ti/Ti_3SiC_2/SiC/Ti_3SiC_2/Ti$, and investigated nonequilibrium quantum transport properties. Figure 22(a) schematically shows a model of the sandwich transport system, which can be divided into a left semi-infinite electrode, a scattering region, and a right semi-infinite electrode. The scattering region consists of hexagonal SiC and Ti_3SiC_2 layers and the periodic boundary conditions are imposed along the directions parallel to the interface. The SiC/Ti_3SiC_2 interface could be either the SiSi or SiCSi, whereas other interfaces are maintained identical for the sandwich systems. In this sense, the difference between the two systems can be mainly attributed to their differing SiC/Ti_3SiC_2 interfaces. Furthermore, we also calculated the Ti/SiC/Ti system, wherein the SiTi model shown in Fig. 15(c) was taken as the SiC/Ti interface.
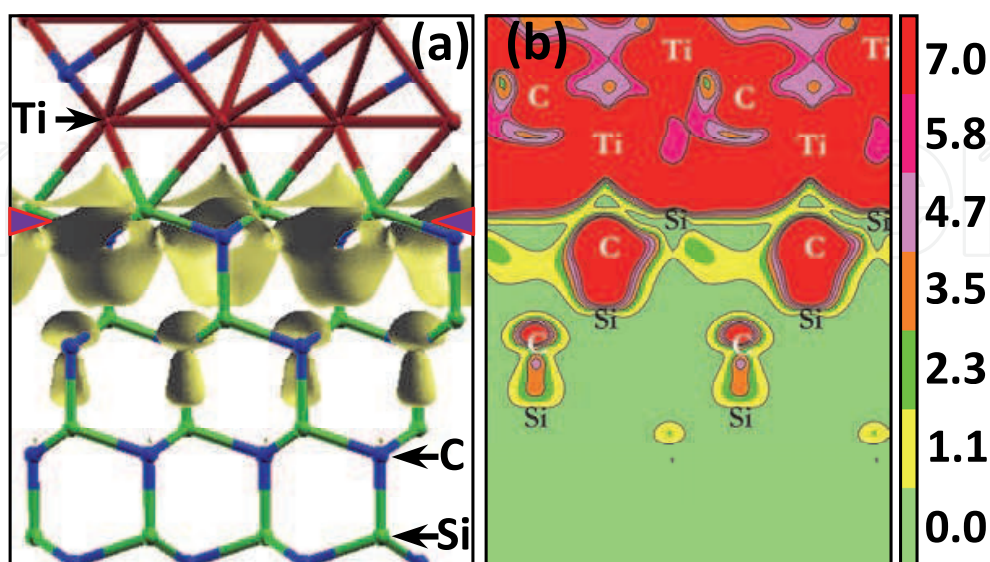

Fig. 21. Isosurface and (b) electron density plot along the (11-20) plane in the energy window (E_F-0.5 eV, E_F) for the SiCSi interface. The interface is marked by two arrows.
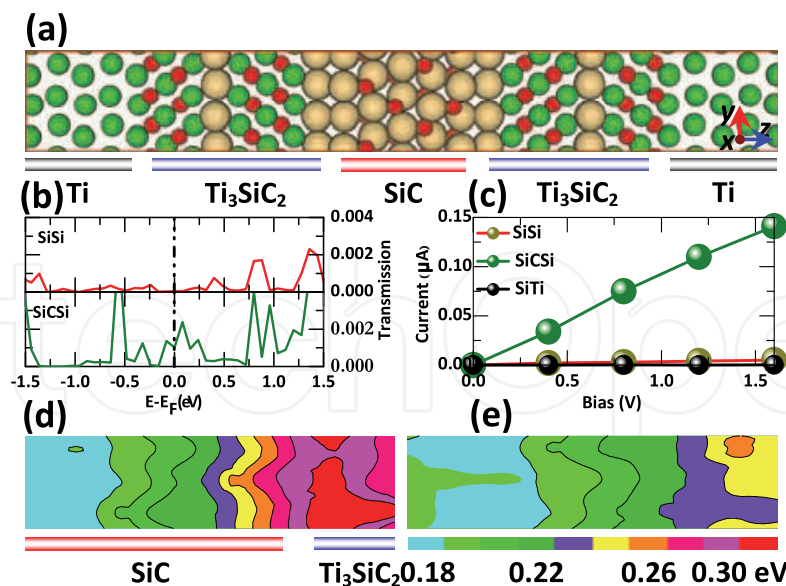
Fig. 22. Schematic plot of a two-probe Ti/Ti₃SiC₂/SiC/Ti₃SiC₂/Ti transport system. The system has infinite extent in the (*x*, *y*) directions and extends to ± ∞ in the *z* direction. (b) Transmission spectra under 0 V and (c) *I-V* curves for the two relaxed systems including the SiSi and SiCSi interfaces. The *I-V* curve for the system including the SiTi interface is also shown for comparison. Difference in effective potential along the (11-20) plane under an applied bias voltage of 0.4 V for (d) SiSi and (e) SiCSi cases

Figure 22(b) shows transmission spectra for the relaxed SiSi, SiCSi, and SiTi systems, where one can see that the spectra differ from one another suggesting variations in electronic structures with interface geometries. The most interesting feature is the presence of transmission peaks at E_F for the SiCSi, which is attributable to the electrons distributed around the interface at E_F. Further calculations on electrical properties (e.g., $I−V$ curve) for the three systems reveal that the current in the SiCSi case increases much faster than either the SiSi or SiTi case as the applied bias voltage increases (Fig. 22(b)), which can be explained by its lowest SBH (Table I). Finally, in comparing the general trend of the calculated $I−V$ with that of the experimental curve (Fig. 1), we find that they agree qualitatively: both the annealed specimen and the SiCSi model clearly show Ohmic behavior, thereby validating the application of the SiCSi model to describe the Ohmic contacts in the TiAl-based system. Finally, we examined how applied bias voltages vary from the interface to the SiC region. Figure 22(d) and (e) illustrate the difference in effective potential along the (11-20) plane between the bias voltage of 0.4 V and the one of 0.0 V for the two relaxed systems including SiSi and SiCSi. One can see that the voltage drops less intensively from interface to SiC in the SiCSi case, suggestive of a less Schottky nature.

4. Discussion and conclusion

The current understanding of formation origin of Ohmic contact, which is based mainly on experimental studies of property measurement and structure characterization, can be summarized in three main points: (1) the deposited Al (80 at%) might diffuse in part into the SiC and dope heavily the semiconductor because Al is well-known to act as a *p*-type dopant for SiC, (2) the high density of pits, spikes, or dislocations may be generated underneath the contacts after annealing so that current can transport primarily through these defects due to

the possible enhancement of electric field at these features and semiconductor doping at these locations, (3) formation of intermediate semiconductor layer between the deposited metals and semiconductor, which consists of silicides or carbides, could divide the high barrier height into lower ones, thus reducing the effective barrier height.

The findings presented first demonstrate that no Al is clearly segregated around the interfacial region, in particular at the top few layers of SiC, which rules out the possibility of additional Al doping. Though a small amount of residual Al is found to be present, mostly in a form of Al_4C_3 compound, it may locate on the surface of annealed contacts rather than in the layer directly contacted to the SiC, thus playing a negligible role in Ohmic contact formation. The majority of deposited Al is evaporated during annealing because of its low melting point and high equilibrium vapor pressure. The dominant role played by Al in the TiAl system is to assist the formation of liquid alloy so as to facilitate chemical reaction. Furthermore, careful characterization of the interfacial region reveals that the substrate and the generated compound are epitaxially oriented and well matched at interface with no clear evidence of high density of defects. This suggests that the morphology might not be the key to understanding the contact formation. In support of this speculation, it has been observed previously that Ti Ohmic contacts can be possibly generated without any pitting and that pit-free Ohmic contacts can be fabricated.

One remaining theory is the alloy-assisted Ohmic contact formation. This alloy is determined to be ternary Ti_3SiC_2, which has also been corroborated by other expriments. Since the bulk Ti_3SiC_2 has already been found to be of metallic nature both in experiment and theory, the contact between Ti_3SiC_2 and its covered metals should show Ohmic character and thus the SiC/Ti_3SiC_2 interface should play a significant role in Ohmic contact formation. This idea is supported by the fact that the determined interface has a lowered SBH due to the large dipole shift at interface induced by the partial ionicity and the considerable charge transfer. In addition, the interfacial states, as indicated by the electron distribution at E_F, are also viewed as a contributing factor in reducing the SBH. These states might be further enhanced by the possible presence of point defects at interface, although these structural defects have not been detected by the TEM study.

The calculations predict that an atomic layer of carbon emerges as the first monolayer of Ohmic contacts, which eventually affects interface electronic structure. Such trapped carbon was previously studied in both other interfacial systems theoretically by DFT and the TiNi Ohmic contacts on 4H-SiC experimentally by Auger electron spectroscopy (Ohyanagi et al., 2008). It was proposed that the carbon could be segregated to interfacial area, strengthening interface substantially and reducing Schottky barrier dramatically. Further, it was reported that the Ohmic contact can be realized by depositing carbon films only onto the SiC substrate, indicative of the determinative role of carbon in the Ohmic contact formation (Lu et al., 2003). The important role played by carbon can be traced to the two interfacial Si layers, which provide possible sites for carbon segregation due to the strong Si-C interaction. Finally, recent observation shows that atomic-scale Ti_3SiC_2-like bilayer can be embedded in the SiC interior, forming an atomically ordered multilayer that exhibits an unexpected electronic state with the point Fermi surface. The valence charge is found to be confined largely within the bilayer in a spatially connected way, which serves as a possible conducting channel to enhance the current flow over the semiconductor.

Several experimental methods can be used to probe the Ohmic character of Ti_3SiC_2 contacts on SiC discussed in this chapter. For example, based on the results regarding morphology of grown layers, epitaxial Ti_3SiC_2 layers can be deposited directly onto the SiC substrate by

means of sputtering, molecular bean epitaxy (MBE), or pulsed-laser deposition (PLD). In particular, the crucial effect of interfacial carbon can be possibly examined using the MBE and PLD techniques, which allow a layer-by-layer deposition of crystalline thin films. If the outcome of such investigations is positive for Ohmic contact formation, direct deposition of epitaxial Ti_3SiC_2 thin films rather than the metals would be a potential processing technique for easier realization of ordered structure and better control of Ohmic property.

To summarize, we have determined in this chapter atomic-scale structure of Ohmic contacts on SiC and related it to electronic structure and electric property, aimed at understanding the formation mechanism of Ohmic contact in TiAl-based system. The combined HAADF-DFT study represents an important advance in relating structures to device properties at an atomic scale and is not limited to the contacts in SiC electronics. Our results show that the main product generated by chemical reaction can be epitaxial and have atomic bonds to the substrate. The contact interface, which could trap an atomic layer of carbon, enables lowered Schottky barrier due to the large interfacial dipole shift associated with the considerable charge transfer. These findings are relevant for technological improvement of contacts in SiC devices, and this chapter presents an important step towards addressing the current contact issues in wide-band-gap electronics.

5. Acknowledgment

6. References

Chang, S. C.; Wang, S. J.; Uang, K. M. & Liou, B. W. (2005). Investigation of Au/Ti/Al Ohmic Contact to N-type 4H-SiC, *Solid State Electronics,* Vol.49, No.12, (December 2005), pp. 1937-1941, ISSN 0038-1101

Ching, W. Y.; Xu, Y. N.; Rulis, P. & Ouyang, L. Z. (2006). The Electronic Structure and Spectroscopic Properties of 3C, 2H, 4H, 6H, 15R and 21R Polymorphs of SiC, *Materials Science and Engineering A,* Vol.422, No.1-2, (April 2006), pp. 147-156, ISSN 0921-5093

Gao, M.; Tsukimoto, S.; Goss, S. H.; Tumakha, S. P.; Onishi, T.; Murakami, M. & Brillson, L. J. (2007). Role of Interface Layers and Localized States in TiAl-Based Ohmic Contacts to p-Type 4H-SiC, *Journal of Electronic Materials,* Vol.36, No.4, (April 2007), pp. 277-284, ISSN 0361-5235

Harries, G. L. (1995). *Silicon Carbide,* INSPEC, ISBN 0-85296-870-1, London, United Kingdom

Johnson, B. J. & Capano, M. A. (2004). Mechanism of Ohmic Behavior of Al/Ti Contacts to p-type 4H-SiC After Annealing, *Journal of Applied physics*, Vol.95, No.10, (May 2004), pp. 5616-5620, ISSN 0021-8979

Käckell, P.; Wenzien, B. & Bechstedt, F. (1994). Electronic Properties of Cubic and Hexagonal SiC Polytypes from ab initio Calculations, *Physical Review B*, Vol.50, No.15, (October 1994), pp. 10761-10768, ISSN 1098-0121

Kresse, G. & Hafner, J. (1993). Ab initio Molecular Dynamics for Liquid Metals, *Physical Review B*, Vol.47, No.1, (January 1983), pp. 558-561, ISSN 1098-0121

Lu, W.; Mitchel, W. C.; Thornton, C. A.; Collins, W. E.; Landis, G. R. & Smith, S. R. (2003), Ohmic Contact Behavior of Carbon Films on SiC, *Journal of The Electrochemical Society*, Vol.153, No.3, (January 2003), pp. G177-G182, ISSN 0013-4651

Mohney, S. E.; Hull, B. A.; Lin, J. Y. & Crofton, J. (2002). Morphological study of the Al-Ti Ohmic Contact to p-type SiC, *Solid State Electronics*, Vol.46, No.5, (May 2002), pp. 689-693, ISSN 0038-1101

Morkoc, H.; Strite, S.; Gao, G. B.; Lin, M. E.; Sverdlov, B. & Burns, M. (1994). Large-band-gap SiC, III-V Nitride, and II-VI ZnSe-based Semiconductor Device Technologies, *Journal of Applied physics*, Vol.76, No.3, (August 1994), pp. 1363-1398, ISSN 0021-8979

Nakatsuka, O.; Takei, T.; Koide, Y. & Murakami, M. (2002). Low Resistance TiAl Ohmic Contacts with Multi-Layered Structure for p-Type 4H-SiC, *Materials Transactions*, Vol.43, No.7, (July 2002), pp. 1684-1688, ISSN 1345-9678

Nellist, P. D.; Chisholm, M. F.; Dellby, N.; Krivanek, O. L.; Murfitt, M. F.; Szilagyi, Z. S.; Lupini, A. R.; Borisevich, A.; Sides, Jr. W. H. & Pennycook, S. J. (2004). Direct Sub-Angstronm Imaging of a Crystal Lattice, *Science*, Vol.305, No.5691, (September 2004), pp. 1741, ISSN 0036-8075

Ohyanagi, T.; Onose, Y. & Watanabe, A. (2008). Ti/Ni Bilayer Ohmic Contact on 4H-SiC, *Journal of Vacuum Science and Technology B*, Vol.26, No.4, (August 2008), pp. 1395-1362, ISSN 1071-1023

Pennycook, S. J. & Boatner L. A. (1988). Chemically Sensitive Structure-Imaging with a Scanning Transmission Electron Microscope, *Nature*, Vol.336, No.6199, (December 1988), pp. 565-567, ISSN 0028-0836

Perez-Wurfl, I.; Krutsinger, R.; Torvik, J. T. & Van Zeghbroeck, B. (2003). 4H-SiC Bipolar Junction Transistor with High Current and Power Density, *Solid State Electronics*, Vol.47, No.2, (February 2003), pp. 229-231, ISSN 0038-1101

Tanimoto, S.; Kiritani, N.; Hoshi, M. & Okushi, H. (2002). Ohmic Contact Structure and Fabrication Process Applicable to Practical SiC Devices, *Materials Science Forum*, Vol.389-393, No.2, (January 2002), pp. 879-884, ISSN 0255-5476

Tsukimoto, S.; Nitta, K.; Sakai, T.; Moriyama, M. &Murakami, M. (2004). Correlation Between the Electrical Properties and the Interfacial Microstructurs of TiAl-Based Ohmic Contacts to p-type 4H-SiC, *Journal of Electronic Materials*, Vol.33, No.5, (May 2004), pp. 460-466, ISSN 0361-5235

Viala, J. C.; Peillon, N.; Bosselet, F. & Bouix, J. (1997). Phase Equilibra at 1000°C in the Al-C-Si-Ti Quaternary system: an Experiemtnal Approach, *Materials Science and Engineering A*, Vol.229, No.1-2, (June 1997), pp. 95-113, ISSN 0921-5093

Wang, X. G.; Smith, J. R. & Evans, A. (2002), Fundamental Inflenence of C on Adhesion of the Al$_2$O$_3$/Al Interface, *Physical Review Letters*, Vol.89, No.28, (December 2002), pp. 286102-1-4, ISSN 0031-9007
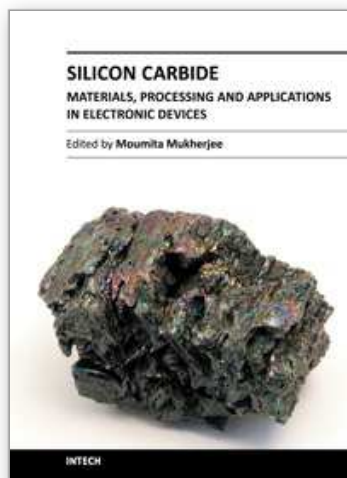
Silicon Carbide - Materials, Processing and Applications in Electronic Devices

Edited by Dr. Moumita Mukherjee

ISBN 978-953-307-968-4

Hard cover, 546 pages

Publisher InTech

Published online 10, October, 2011

Published in print edition October, 2011

Silicon Carbide (SiC) and its polytypes, used primarily for grinding and high temperature ceramics, have been a part of human civilization for a long time. The inherent ability of SiC devices to operate with higher efficiency and lower environmental footprint than silicon-based devices at high temperatures and under high voltages pushes SiC on the verge of becoming the material of choice for high power electronics and optoelectronics. What is more important, SiC is emerging to become a template for graphene fabrication, and a material for the next generation of sub-32nm semiconductor devices. It is thus increasingly clear that SiC electronic systems will dominate the new energy and transport technologies of the 21st century. In 21 chapters of the book, special emphasis has been placed on the â€œmaterialsâ€ aspects and developments thereof. To that end, about 70% of the book addresses the theory, crystal growth, defects, surface and interface properties, characterization, and processing issues pertaining to SiC. The remaining 30% of the book covers the electronic device aspects of this material. Overall, this book will be valuable as a reference for SiC researchers for a few years to come. This book prestigiously covers our current understanding of SiC as a semiconductor material in electronics. The primary target for the book includes students, researchers, material and chemical engineers, semiconductor manufacturers and professionals who are interested in silicon carbide and its continuing progression.

How to reference

In order to correctly reference this scholarly work, feel free to copy and paste the following:

INTECH
open science | open minds

www.intechopen.com